

Reassessing iron–gallium recombination activity in silicon

Cite as: J. Appl. Phys. **135**, 133107 (2024); doi: [10.1063/5.0198737](https://doi.org/10.1063/5.0198737)

Submitted: 19 January 2024 · Accepted: 19 March 2024 ·

Published Online: 3 April 2024



Tien T. Le,^{1,a)} Zhuangyi Zhou,² Alan Chen,¹ Zhongshu Yang,¹ Fiacre Rougieux,² Daniel Macdonald,¹ and AnYao Liu^{1,a)}

AFFILIATIONS

¹School of Engineering, College of Engineering, Computing and Cybernetics, The Australian National University, Canberra ACT 2601, Australia

²School of Photovoltaic and Renewable Energy Engineering, The University of New South Wales, Australia

^{a)}Authors to whom correspondence should be addressed: tien.le@anu.edu.au and anyao.liu@anu.edu.au

ABSTRACT

In this work, we present a comprehensive re-evaluation of the iron–gallium (FeGa) recombination parameters in silicon using injection-dependent lifetime spectroscopy (IDLS). Ga-doped silicon wafers (of varying resistivities) with precise concentrations of intentional iron contamination in the silicon wafer bulk, through ion implantation and distribution, were used. The presence of interstitial Fe_i and FeGa, and their lifetime-limiting effects in these silicon wafers, were confirmed through measuring the effective minority carrier lifetime changes during the conditions that are known to cause FeGa dissociation and association. The presence of Fe was also confirmed by deep-level transient spectroscopy. To ensure accurate IDLS analysis of the FeGa defect in silicon, a lifetime linearization scheme was employed to effectively filter out interference by other defects. Error analysis was employed to find the combination of defect parameters that best fit the experimental data and to ascertain the range of uncertainty associated with the IDLS best-fit results. The optimal fitting of the experimental IDLS by Shockley–Read–Hall statistics produced an electron capture cross section $\sigma_n = 2.3 \times 10^{-14} \text{ cm}^2$, hole capture cross section $\sigma_p = 1.1 \times 10^{-14} \text{ cm}^2$, and a trap energy level $E_t = E_V + 0.2_{-0.01}^{+0.02} \text{ eV}$ for the FeGa defect in silicon. The extracted defect parameters are also verified by experimentally measuring the crossover point of Fe_i and FeGa lifetime curves.

© 2024 Author(s). All article content, except where otherwise noted, is licensed under a Creative Commons Attribution (CC BY) license (<https://creativecommons.org/licenses/by/4.0/>). <https://doi.org/10.1063/5.0198737>

I. INTRODUCTION

The silicon photovoltaic (PV) sector has recently witnessed a rapid and significant shift in the primary dopant element for *p*-type Czochralski-grown silicon (Cz-Si) wafers, transitioning from boron (B) to gallium (Ga).¹ The increasing interest in Ga-doped wafers stems from their numerous advantages, notably their effectiveness in avoiding light-induced degradation due to the boron-oxygen defect.^{2–4} Although boron-oxygen is absent in Ga-doped silicon wafers, the presence of metal impurities, particularly iron (Fe), remains a persistent concern in Cz-Si wafers.^{5–8}

As a notorious impurity in Si, the formation of a metastable complex of Fe and Ga in silicon, FeGa, has been reported previously.^{9–17} Upon illumination, these FeGa complexes can dissociate into interstitial iron (Fe_i) and substitutional Ga,¹⁸ similar to the well-known iron–boron (FeB) pairs in silicon.^{9,11,19} Under dark

conditions, Fe_i and the acceptor dopant (B or Ga) re-pair quickly (within minutes or hours, depending on the dopant concentration), with a re-pairing rate that is determined by the Fe_i diffusivity in silicon.^{20,21}

There is a range of data reported in the literature regarding the recombination activity of the iron–gallium (FeGa) defect in silicon, both in terms of its electron and hole capture cross sections and defect energy level.^{10–17} In fact, two different groups of structural configurations have been reported for FeGa in Si: one is trigonal with an energy level (E_t) near 0.20–0.25 eV above the valence band (E_V),^{9–16} and the other is orthorhombic with its energy level located at 0.09–0.15 eV above E_V .^{10,14–17}

However, there are conflicting results in the literature regarding which configuration dominates the recombination activity of FeGa in silicon.¹⁰ Some studies detected only the deeper trigonal

06 April 2024 05:59:45

trap (0.20–0.25 eV) as the dominant recombination center, and for these studies Fe was introduced into Si through either ion implantation^{9,12} or surface contamination and annealing.^{11,13} A similar approach of surface scraping combined with thermal annealing,¹⁴ and another study based on purposely introducing Fe during silicon ingot growth,²² reported both trigonal and orthorhombic states of FeGa.

On the other hand, investigations using as-grown Ga-doped Cz silicon wafers with varying solidified fractions, without intentionally introducing Fe, were conducted to assess the recombination activity of FeGa.^{10,15} They concluded that the shallower orthorhombic configuration ($E_t = E_V + 0.09$ eV) of FeGa is the predominant recombination center.¹⁰ This conclusion, however, strongly depends on the assumption that Fe is the main lifetime-limiting defect in these gallium-doped silicon wafers.

As the recombination parameters of FeGa are crucial for accurately measuring the dissolved Fe concentrations in Ga-doped Si wafers and for assessing the impact of FeGa defects on device performance, it is important to reassess the FeGa defect parameters. In this study, we apply injection-dependent lifetime spectroscopy (IDLS), (e.g., 23 and 24) to reassess the Shockley–Read–Hall (SRH) recombination parameters of FeGa in Si, namely, the electron and hole capture cross sections (σ_n and σ_p) and the defect energy level (E_t). Samples with varying FeGa concentrations (i.e., defect density, N_t , in SRH statistics) and varying doping concentrations (N_A) were prepared. Fe was introduced into the Ga-doped Si wafers by ion implantation and annealing, and the presence of Fe in the Si wafers was confirmed by assessing the FeGa pairing kinetics^{20,21} as well as through deep-level transient spectroscopy (DLTS) measurements. We adopted the lifetime parameterization method by Murphy *et al.*²⁵ to eliminate the possible interference of other defects on the lifetime data. The impacts of surface and other defects have also been considered. Sensitivity analysis and defect parameter (σ_n , σ_p and E_t) contour mapping are carried out to find the set of defect parameters, which best fit the experimental data, as well as the uncertainty range of the extracted parameters. The extracted defect parameters are also verified by experimentally measuring the crossover point of Fe_i and FeGa lifetime curves. Finally, the predicted effects of the new recombination parameters on lifetime-based Fe_i measurements and the SRH lifetime curves are presented.

II. METHODOLOGY

A. Experimental details

The Ga-doped Cz-Si wafers in this study were sourced from the PV industry. The wafers had six different resistivity values: 8.4, 5.5, 0.92, 0.80, 0.55, and 0.26 Ω cm, and were approximately 170 ± 10 μm thick (except for the 0.92 Ω cm wafer, which had a thickness of 230 ± 10 μm). A 4 μm per side saw damage removal was carried out using tetramethylammonium hydroxide (TMAH) etching, followed by standard Radio Corporation of America (RCA) cleaning procedures. Subsequently, the wafers underwent a heavy phosphorus diffusion process (POCl_3 gettering) to getter existing metallic impurities in the as-grown Cz-Si wafers, to minimize their influence on the measured effective lifetimes, which should ideally be dominated by FeGa after Fe implantation. Phosphorus diffusion was carried out using a POCl_3 source in a

quartz-tube furnace, with the deposition at 770 $^\circ\text{C}$ for 20 min, followed by a 900 $^\circ\text{C}$ drive-in for 30 min, with both ramping up and cooling down controlled at a rate of 5 $^\circ\text{C}$ per minute to 700 $^\circ\text{C}$. This step resulted in a sheet resistivity of 25 Ω/\square . Afterward, another TMAH etching step was performed to remove the diffused layer at approximately 5 μm per side.

These phosphorus pre-gettered wafers then underwent iron ion implantation with surface doses of 1.6×10^{11} , 1.12×10^{11} , 0.80×10^{11} , and 0.32×10^{11} cm^{-2} , which would result in bulk Fe concentrations ranging from 0.14×10^{13} to 1.0×10^{13} cm^{-3} after Fe distribution. Annealing was used to distribute Fe throughout the Si wafer thickness.²⁶ Details of this controlled Fe contamination process can be found in our previous work.^{26–28} Following this distribution annealing, the Fe samples, along with the co-processed control wafers without Fe implantation (but with pre-gettering and annealing), were subjected to another TMAH etching to remove any potential surface damage caused by ion implantation.

Subsequently, RCA cleaning was performed before thermal deposition of aluminum oxide (AlO_x) thin films on both sides of the wafer surfaces using the atomic layer deposition (ALD) technique. Thermal AlO_x films were deposited at 200 $^\circ\text{C}$ using a Beneq TFS 200 series reactor.²⁹ The films were prepared by alternating trimethylaluminum (TMA) exposure and H_2O for 200 cycles. Following ALD, both the Fe and control samples received an additional forming gas anneal (FGA) at 400 $^\circ\text{C}$ for 30 min to activate the AlO_x films.²⁹ The AlO_x films had a thickness of approximately 20 nm. While plasma-assisted ALD AlO_x was found to have gettering effects for Fe,^{30,31} the thermal AlO_x used in this study did not exhibit noticeable Fe gettering effects.

The effective minority carrier lifetime curves (in other words, IDLS lifetime curves) of the AlO_x passivated samples were measured by a photoconductance-based lifetime tester (WCT-120, Sinton Instruments) at room temperature.³² The temperature of the measurement stage was approximately 30 $^\circ\text{C}$. The generalized 1/1 mode was used to analyze all samples with lifetimes less than 100 μs , while the transient mode was applied to analyze control samples with lifetimes exceeding 200 μs , following the recommendations in the Sinton measurement manual. Additionally, samples with lifetimes falling within the range of 100–200 μs were also analyzed using the generalized 1/1 mode.

To confirm the presence of Fe in the ion-implanted samples, the FeGa pair association process was monitored to quantify the association time constants, and then to compare those with the literature reported Fe-acceptor association time constants in *p*-type Si.^{20,21} The samples were initially left in the dark for at least 24 h to allow FeGa to be fully paired, as reflected by their measured lifetimes being unchanged after further storing in the dark. Subsequently, the samples were exposed to illumination on a temperature-controlled stage (to avoid overheating), using a direct light source until no further increase in carrier lifetime was observed, indicating a fully dissociated state. Following this, the samples were returned to the dark condition, and periodic measurements of the carrier lifetime were conducted until the lifetime becomes unchanged again, indicating the FeGa fully paired state. Care was taken to avoid strong flashing during measurement, and this pair association experiment was repeated for each sample at least once to ensure reproducibility of the results. Applying the

06 April 2024 05:59:45

same approach as in Refs. 20 and 21, the association time constants of the ion-implanted samples were measured. While the experiment has been designed to minimize the partial dissociation of FeGa to Fe_i, we acknowledge that there may still be a small, unknown fraction of Fe_i dissociated during the measurement process. This unknown portion is neglected in this work.

An additional confirmation of the presence of Fe in the ion-implanted Si wafers was established through DLTS measurements. In preparation for Schottky barrier diodes (SBDs) for DLTS measurements, the samples were mechanically polished using a Tegramin-25 tool from Struers. This step was applied to reduce the leakage current of the SBDs as well as to obtain an accurate area for capacitance–voltage (CV) measurements to estimate the doping concentration and the defect densities. Approximately 10 μm of material was removed including the AlO_x layer on the front. The polished samples were then cleaned with RCA solutions followed by hydrofluoric acid (HF) dip until hydrophobic. AlO_x on the rear side was removed in this step. Finally, Schottky contacts were formed using aluminum and Ohmic contacts were formed using gold. Aluminum was evaporated using an e-beam evaporator tool Lesker physical vapor deposition (PVD) 75 with a 1 mm diameter circle shadow mask covered on the polished sides of the samples; gold was evaporated using a Lesker thermal evaporator on the full area of the rear sides. The quality of SBDs was examined based on current–voltage (IV) and CV results at room temperature. The leakage current at 10 V reverse bias was below 1×10^{-4} A and the fitted doping concentration aligns with the expected values (measured with a Sinton lifetime tester). DLTS measurements were conducted from 100 to 300 K using a HERA DLTS tool from PhysTech and the defect densities were analyzed based on the amplitudes of the defect peaks and CV results.

The lifetimes in the FeGa fully paired state were used for extracting the defect parameters using IDLS. The consistency of the lifetime data was checked by cycling between the Fe_i and FeGa states via light and dark storage, as described above.

B. SRH defect parameterization by IDLS

1. Lifetime due to FeGa

The effective lifetime of the samples in the fully paired FeGa state can be expressed as

$$\frac{1}{\tau_{\text{eff, FeGa}}} = \frac{1}{\tau_{\text{intrinsic}}} + \frac{1}{\tau_{\text{surface}}} + \frac{1}{\tau_{\text{SRH, others}}} + \frac{1}{\tau_{\text{residual, FeGa}}}, \quad (1)$$

where $\tau_{\text{eff, FeGa}}$ is the measured effective lifetime for the Fe-implanted samples in the FeGa fully paired state; $\tau_{\text{intrinsic}}$ is the intrinsic lifetime;^{33,34} τ_{surface} is the lifetime due to surface recombination; $\tau_{\text{SRH, others}}$ is the bulk SRH lifetime which stems from defects other than FeGa; and $\tau_{\text{residual, FeGa}}$ is the lifetime due to FeGa.

Please note that in this work, $\tau_{\text{residual, FeGa}}$ denotes the experimentally measured FeGa lifetime, while $\tau_{\text{SRH, FeGa}}$ is used to denote the simulated FeGa lifetime using the best-fit defect parameters.

For the control samples with no Fe implantation, the last term in Eq. (1), $\frac{1}{\tau_{\text{residual, FeGa}}}$ is negligible due to effective pre-gettering to remove residual Fe. As the control samples were co-processed with

the Fe samples, it is reasonable to assume that the first three terms in Eq. (1), $\tau_{\text{intrinsic}}$, τ_{surface} , and $\tau_{\text{SRH, others}}$, are the same for the Fe and control samples. Hence, the experimental lifetime due to FeGa, $\tau_{\text{residual, FeGa}}$, can be then expressed as

$$\frac{1}{\tau_{\text{residual, FeGa}}} \approx \frac{1}{\tau_{\text{eff, FeGa}}} - \frac{1}{\tau_{\text{eff, control}}}, \quad (2)$$

where $\tau_{\text{eff, control}}$ is the measured effective lifetime of the co-processed control samples.

Assuming FeGa is the bulk-limiting defect (we will examine this in Sec. III B2), $\tau_{\text{residual, FeGa}}$ from Eq. (2) is used to determine the SRH recombination parameters of FeGa.

2. Murphy's linearization scheme for data filtering

According to Ref. 25, the Shockley–Read–Hall (SRH) lifetime equation can be rearranged into a linear form when plotting the residual minority carrier lifetime against the ratio of electron to hole carrier concentrations (n/p in p -type Si or p/n in n -type Si). This linearization of experimentally obtained injection-dependent lifetime curves demonstrates that a linear lifetime curve (after linearization rearrangement) emerges exclusively in scenarios where a singular recombination center predominates. On the other hand, a non-linear lifetime curve after rearrangement, particularly, suggests either the existence of a single defect with dual recombination levels or two separate defects with a single-level each.²⁵ Consequently, to ensure the suitability of the “input” lifetime curves for IDLS analysis and to mitigate the interference from other defects, this linearization approach has been employed as a data selection criterion. This criterion filters out experimental $\tau_{\text{residual, FeGa}}$ lifetime data that do not conform to a linear curve post-rearrangement, as prescribed in Ref. 25.

3. Fitting of SRH defect parameters to experimental data

The SRH lifetime is ultimately a function of only three unknown parameters: σ_n , σ_p , and E_t . The goal of fitting the simulated SRH lifetime ($\tau_{\text{SRH, FeGa}}$) to the experimentally measured lifetime curves ($\tau_{\text{residual, FeGa}}$) is therefore to find a combination of σ_n , σ_p , and E_t that results in the least average error,

$$\text{Average error} = \frac{\sum_{j=1}^m \left(\sum_{i=1}^n \frac{|\tau_{\text{residual, FeGa}, j} - \tau_{\text{SRH, FeGa}, j}|}{\tau_{\text{residual, FeGa}, j}} \right)}{m} \quad (3)$$

where n is the number of injection level values and m is the number of samples [with different combinations of doping (N_A) and trap concentrations (N_t)] taken into account.¹⁰ In simulating $\tau_{\text{SRH, FeGa}}$, the FeGa trap concentration N_t comes from the known implantation doses of the samples, as we have repeatedly confirmed in our previous studies that the resulting bulk Fe concentration agrees well with the implanted Fe dose through a careful annealing process.^{26,28}

The least error (i.e., best fit) was found by minimizing the average error utilizing the Solver function in Microsoft Excel.³⁵ The defect parameter contour mapping (DPCM) technique¹⁰ was

employed to visualize the uncertainties associated with the extracted best-fit SRH recombination parameters. This involved first fixing the defect energy level at $E_t = E_V + 0.2$ eV (to be explained below) and mapping the calculated average errors against both varying σ_n and σ_p . As will be shown later in Sec. III, this led to the determination of σ_n as fitting is highly sensitive to σ_n . Then, fixing σ_n to the obtained value, the average errors against E_t and σ_p were analyzed to find the best fit E_t and σ_p .

As will be shown later in Sec. III B 1, using the defect parameters of Nærland *et al.*¹⁰ at the energy level of $E_t = E_V + 0.09$ eV produces the FeGa SRH lifetimes which are two orders of magnitude higher than the measured effective lifetimes. Similar results were found for other combinations of the reported σ_n and σ_p if choosing E_t near $E_V + 0.09$ eV. On the other hand, using the defect energy level near $E_t = E_V + 0.2$ eV can closely approximate the experimental lifetimes, albeit giving slight underestimations if using the exact defect parameters from Ref. 9. This led to initially fixing E_t at $E_t = E_V + 0.2$ eV in error analysis, as described above.

Similar to FeB,^{36,37} with the knowledge of the recombination parameters of FeGa and Fe_i, the Fe_i concentration in silicon wafers can be determined by^{36,37}

$$[Fe_i] = C \times \left(\frac{1}{\tau_{\text{eff}, Fe_i}} - \frac{1}{\tau_{\text{eff}, FeGa}} \right) \quad (4)$$

where τ_{eff, Fe_i} and $\tau_{\text{eff}, FeGa}$ are the effective lifetimes in the FeGa fully dissociated (i.e., Fe_i) and fully associated (i.e., FeGa) states, and the

prefactor C is related to the recombination parameters of Fe_i and FeGa, dopant concentration N_A and the injection level.^{36,37}

Note that the thermal velocity (v_{th}) is chosen as $v_{th} = 1.1 \times 10^7$ cm/s for all of the calculations in this study.⁹

III. RESULTS AND DISCUSSION

A. Confirmation of the presence of Fe in Si wafers

To confirm the presence of Fe, we first monitored the lifetime changes upon illumination (to break FeGa pairs into Fe_i and Ga_s) and subsequent dark storage (to allow FeGa re-pairing), as detailed previously in Sec. II A. If the lifetime changes were due to FeGa pair association, the measured time constants of the $[Fe_i]/[Fe_{\text{total}}]$ ratios (inferred from the lifetime changes^{20,21}) would follow the following expression for the association time constant ($\tau_{\text{association}}$), which is related to the Fe diffusivity in silicon:²¹

$$\tau_{\text{association}} = 5.7 \times 10^5 \times \frac{T}{N_A} \times \exp\left(\frac{0.66 \text{ eV}}{kT}\right), \text{ second} \quad (5)$$

where T is the measurement temperature, N_A is the dopant concentration, and k is the Boltzmann constant.

The experimentally measured association time constants were found to agree very well with the expected values from Eq. (5). An example is illustrated in Fig. 1(a). We also tested the association time constants of Fe-implanted boron-doped silicon wafers, and good agreement between experimental time constants and Eq. (5) could be found as well.

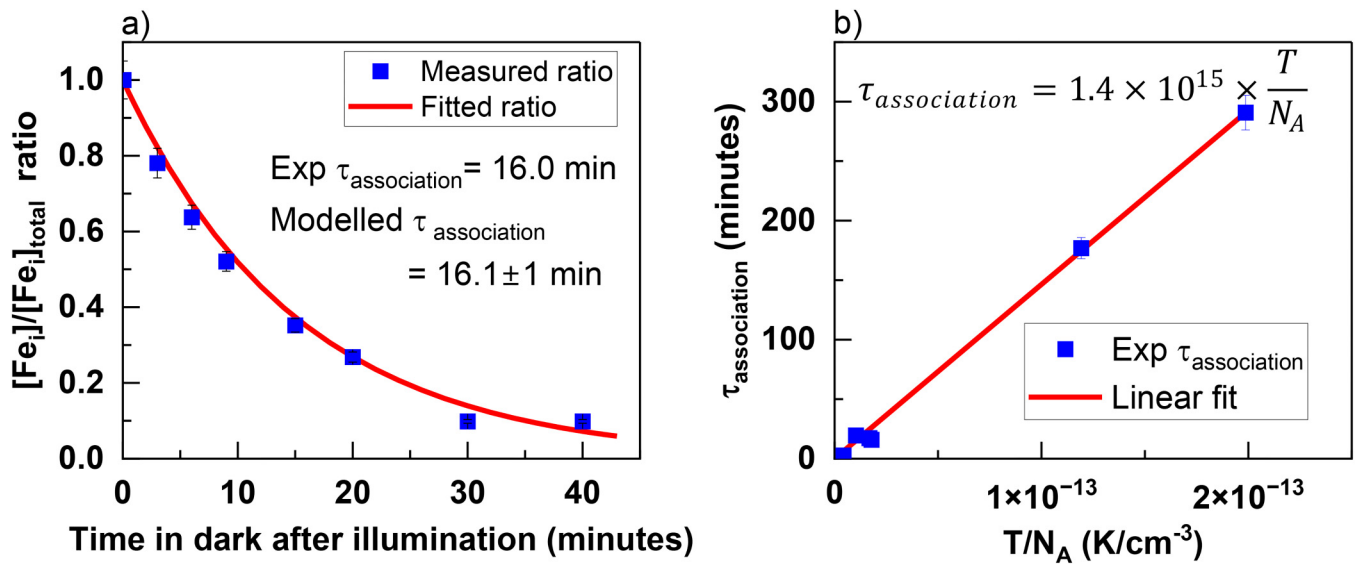


FIG. 1. (a) Time evolution of the $[Fe_i]/[Fe_{\text{total}}]$ ratio, starting from the fully dissociated state as Fe_i (via illumination) and gradually reaching fully associated state of FeGa (via dark storage), on a sample with a resistivity of $0.92 \Omega \text{ cm}$ and an Fe concentration of $N_i = 0.68 \times 10^{13} \text{ cm}^{-3}$. The solid line represents an exponential decay curve fitting to extract the association time constant. The uncertainty in the modeled $\tau_{\text{association}}$ from Ref. 21 was estimated by assuming ± 1 K in the measured temperature of 303 K; (b) experimentally measured $\tau_{\text{association}}$ from a number of samples of different doping (N_A), plotted as a function of the T/N_A ratio. The solid line is a linear fit to the data, and the fitting equation is shown in the plot.

06 April 2024 05:59:45

The experimentally extracted association time constants from samples with a range of resistivities are plotted in Fig. 1(b). The fitting of experimental $\tau_{\text{association}}$ vs $\frac{T}{N_A}$ results in a slope of $1.4 \times 10^{15} \frac{\text{s}}{\text{cm}^3 \text{K}}$. Considering a temperature range of 298–303 K in experiments, the slope of $\tau_{\text{association}}$ vs $\frac{T}{N_A}$ is in the range of $9.0 \times 10^{14} - 1.4 \times 10^{15} \frac{\text{s}}{\text{cm}^3 \text{K}}$ in Eq. (5). The experimental data from this work therefore closely align with those reported by Tan *et al.*,²¹ i.e., Eq. (5). These results thus provide clear evidence for the presence of Fe in the implanted Si wafers.

In addition, the results confirm that the steady state lifetimes after dark storage are due to FeGa in the fully paired state, as they closely follow the known pairing kinetics. The “dark” lifetimes are therefore suitable for subsequent IDLS analysis to extract the defect parameters of FeGa in Si.

The presence of Fe in the implanted Si wafers was additionally confirmed through DLTS measurements, as illustrated in Fig. 2. The sample had an implanted Fe_i concentration of $7.0 \times 10^{12} \text{ cm}^{-3}$, determined from the ion implantation dose. In the DLTS spectrum [Fig. 2(a)], the H250 peak is attributed to Fe_i , the same as in Ref. 38, as explained as follows. The activation energy and apparent hole capture cross section of the trap H250 were extracted from the T^2 -corrected Arrhenius plot in Fig. 2(b). The energy level of this defect was identified at $E_t = E_V + 0.38 \text{ eV}$, with a measured hole capture cross section $\sigma_p = 6.2 \times 10^{-17} \text{ cm}^2$. These values align well with the previously reported defect parameters of Fe_i in Si.¹⁸ Furthermore, the defect concentration from DLTS was $6.6 \times 10^{12} \text{ cm}^{-3}$, indicating a very small deviation from the implanted dose of Fe in this silicon wafer. Hence, the DLTS measurements of Fe_i serve to corroborate the presence of Fe in the

Si wafers. Nevertheless, further studies are required to confirm the DLTS features related to FeGa.

B. SRH recombination parameters of FeGa

1. Lifetime linearization for data filtering

Figure 3 illustrates an example of the application of Murphy's linearization method for data filtering in the FeGa analysis. Linearization was applied to the experimental residual lifetime data, $\tau_{\text{residual, FeGa}}$ from Eq. (2), which has already subtracted the influence of intrinsic and surface lifetimes. Figure 3(a) shows the rearranged lifetime for a sample in the fully associated state of FeGa after sufficient storing in the dark (majority of FeGa and negligible Fe_i). The rearranged data demonstrate a clear linear line, indicating the presence of a single dominant deep trap.²⁵ In contrast, Fig. 3(b) plots the rearranged lifetime data of a sample in the state of incomplete FeGa association, meaning that there are both isolated Fe_i and FeGa traps within the sample, aligning with the scenario of two single-level defects in Ref. 25. As expected from Ref. 25, the rearranged lifetime curve is not linear.

The implementation of Murphy's linearization method enables filtering out non-linear lifetimes that may be influenced by incomplete pairing or other defects, such as bulk defects, surface defects (that are not reflected in the co-processed control samples, such as surface scratching), or other lifetime artefacts. This filtering process therefore ensures the reliability of the input lifetime data for IDLS model fitting and thus the FeGa recombination activity analysis in this works.

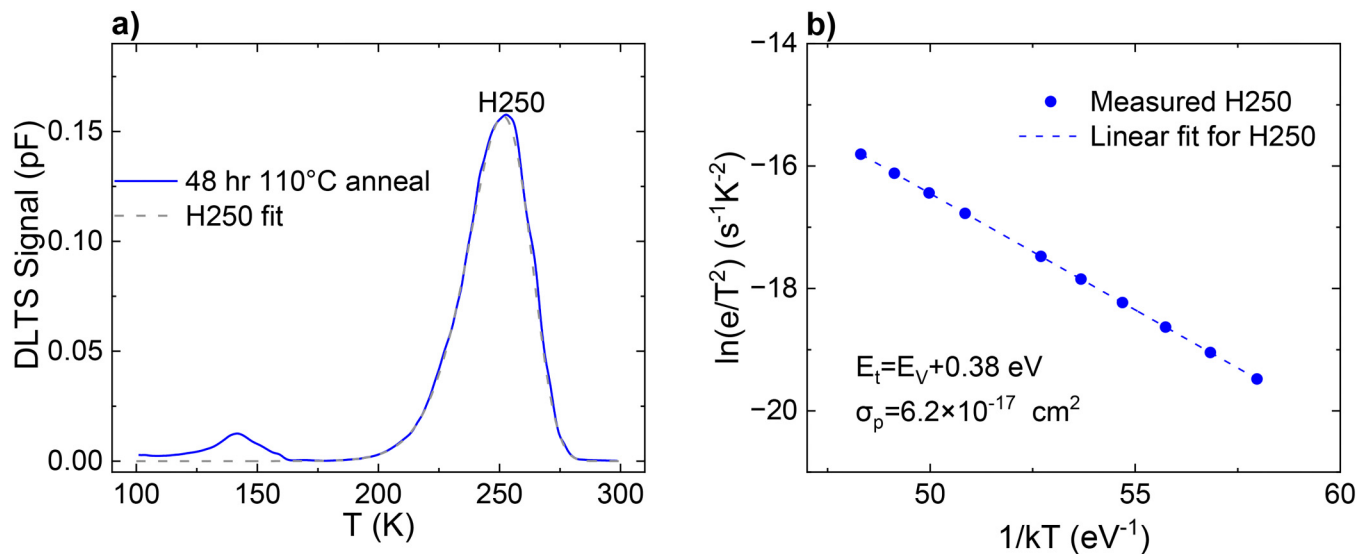


FIG. 2. (a) DLTS spectrum from an Fe-implanted sample ($N_A = 1.8 \times 10^{15} \text{ cm}^{-3}$) with a bulk Fe_i concentration of $7.0 \times 10^{12} \text{ cm}^{-3}$ (determined from the ion implantation dose) after a 48-h 110 °C anneal to dissociate FeGa pairs. The DLTS measurement conditions were as follows: reverse bias voltage (U_r) = −5 V, filling pulse voltage (U_p) = −0.5 V, filling pulse length (t_p) = 1 ms, and period width (T_w) = 20 ms. The solid line is the measured DLTS data, and the dashed line represents the simulated H250 spectrum based on the parameters from (b). (b) An Arrhenius plot of T^2 -corrected emission rates of the H250 peak in (a). The dashed line is a linear fit of the corresponding measured emission.

06 April 2024 05:59:45

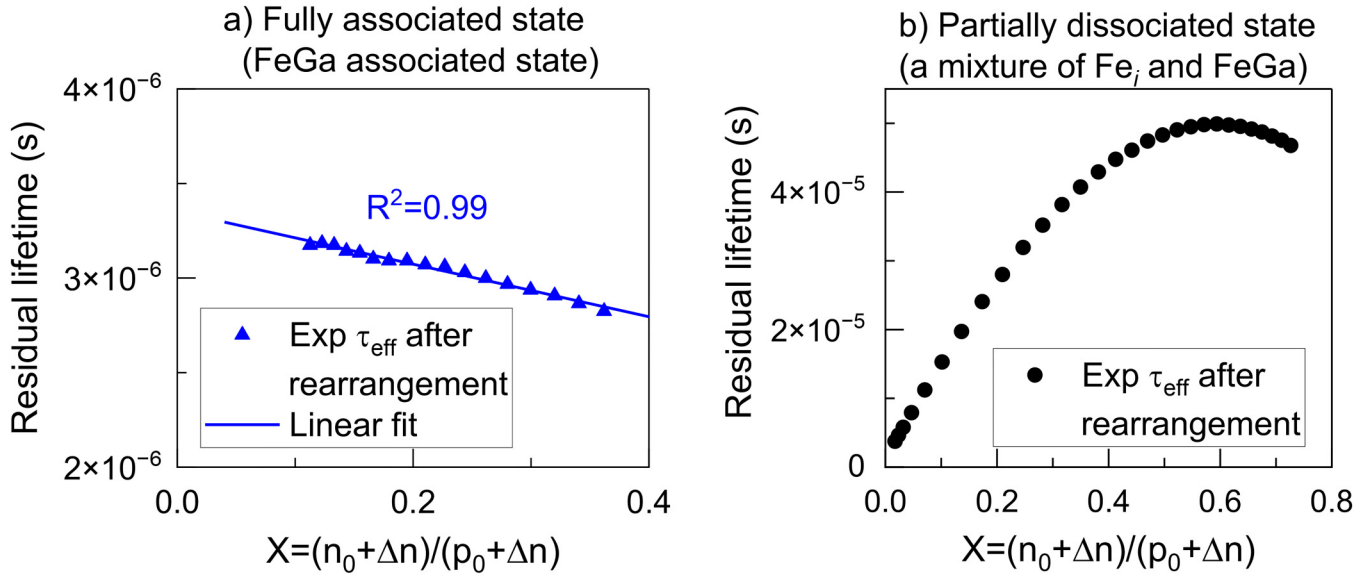


FIG. 3. Examples of injection-dependent lifetime curves [residual lifetime from Eq. (2)] after linearization rearrangement.²⁵ (a) Rearranged lifetime curve in the FeGa fully associated state. The linear fit exhibits a high R^2 value of 0.99, indicating good linearity of the lifetime data. (b) Rearranged lifetime from an Fe-sample in the state of partial FeGa association, that is, there was a mixture of Fe_i and FeGa. A non-linear curve after rearrangement is observed.

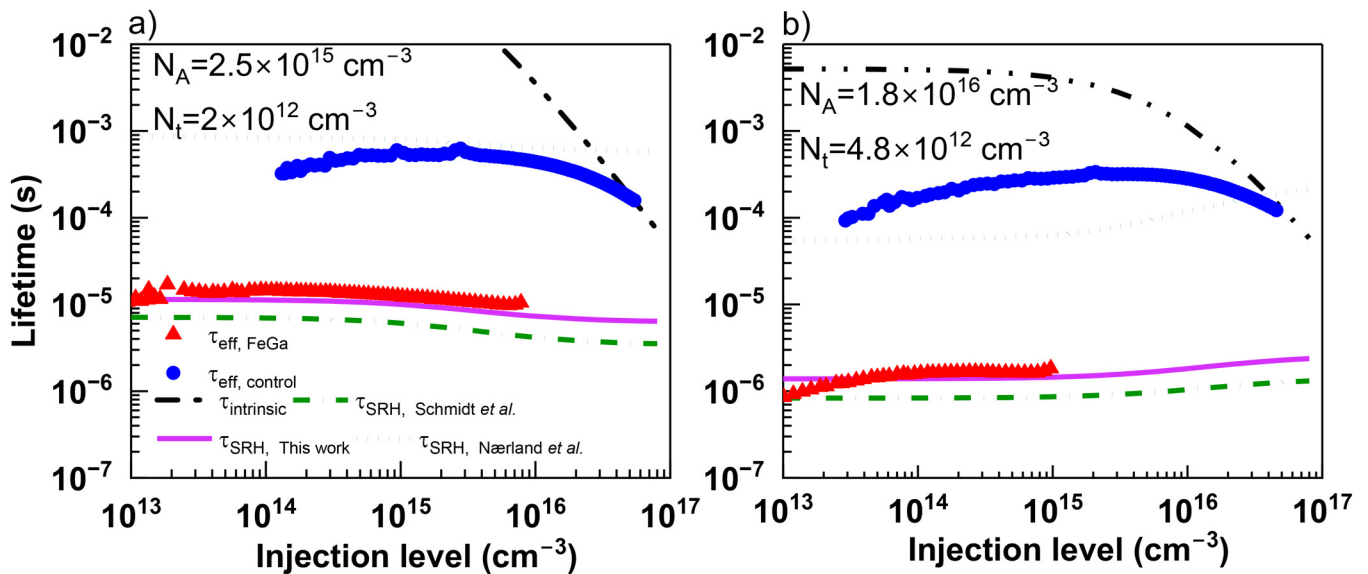


FIG. 4. Experimental and simulated injection-dependent lifetime curves for two sets of samples: Fe-implemented samples in the FeGa paired state, and co-processed control samples with no Fe implantation. The FeGa and control samples in (a) had $N_A = 2.5 \times 10^{15} cm^{-3}$ and $N_t = 2 \times 10^{12} cm^{-3}$, and the samples in (b) had $N_A = 1.8 \times 10^{16} cm^{-3}$ and $N_t = 4.8 \times 10^{12} cm^{-3}$. The simulated lifetimes included intrinsic lifetime,^{33,34} and the SRH lifetimes due to FeGa based on different defect parameters: from this work, Schmidt *et al.*⁹ and Nærland *et al.*¹⁰

TABLE I. A summary of the reported FeGa recombination parameters, from this work and from the literature, determined by various methods, including DLTS, temperature-dependent lifetime spectroscopy (TIDLS), and IDLS.^{a,b}

Authors	Energy level ($E_t - E_V$) eV	σ_n (cm ²)	σ_p (cm ²)	$k = \frac{\sigma_n}{\sigma_p}$	Method	Reference
FeGa trigonal state ($E_t - E_V$) ≈ 0.2 eV						
This work	0.2	2.3×10^{-14}	1.1×10^{-14}	2.1	IDLS	
Schmidt and Macdonald	0.2	4.0×10^{-14}	2.0×10^{-14}	2.0	IDLS	9
Post <i>et al.</i>	0.2	2.5×10^{-14}	1.25×10^{-14}	2.0	IDLS	39
Ciszek <i>et al.</i>	0.21	...	6×10^{-15}	...	DLTS	22
Yoon <i>et al.</i>	0.23	...	5.5×10^{-15}	...	DLTS	15
Dahl <i>et al.</i>	0.26	DLTS	12
Chantre <i>et al.</i>	0.23	DLTS	14
Graff and Pieper	0.25	DLTS	11
Lemke	0.24	...	3×10^{-15}	...	DLTS	40
FeGa orthorhombic state ($E_t - E_V$) ≈ 0.1 eV						
Nærland <i>et al.</i>	0.09	1.9×10^{-14}	7.9×10^{-17}	~ 240	TIDLS	10
Yoon <i>et al.</i>	0.13	...	2.5×10^{-14}	...	DLTS	15
Graff	0.14	DLTS	13 and 17
Chantre <i>et al.</i>	0.14	DLTS	14

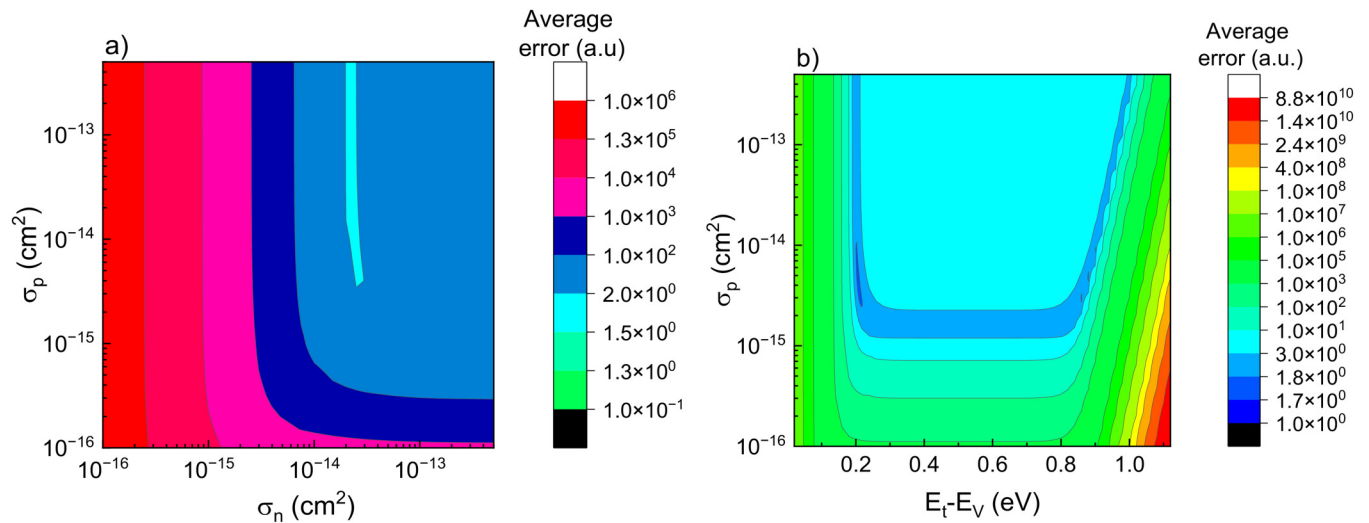
^aNote that caution must be taken when comparing the capture cross sections from DLTS and IDLS. Neglecting or wrongly assuming the temperature dependence of the capture cross sections could lead to deviations of several orders of magnitude in the apparent defect parameters from DLTS, as pointed out by Juhl *et al.*⁴¹ Commonly, the parameters extracted from lifetime spectroscopy (i.e., IDLS or TIDLS) have a significantly lower uncertainty than the apparent parameters from DLTS.⁴¹

^bThe capture cross sections from this work, Schmidt and Macdonald, Post *et al.*, and Nærland *et al.* can be directly comparable with each other, as the SRH formulas use the same thermal velocity for electrons and holes of 1.1×10^7 cm/s, as given in Ref. 42.

2. Experimental lifetime measurements

Figure 4 presents the measured effective lifetimes of two groups of samples (of different doping and FeGa concentrations) after sufficient dark storage, with and without Fe implantation, which are denoted as $\tau_{\text{eff,FeGa}}$ and $\tau_{\text{eff,control}}$, respectively. Figure 4

clearly shows that the lifetimes of the control samples are approximately two orders of magnitude higher than the lifetimes of the FeGa samples. This is the case for most of the samples investigated in this study except for the highest doping 0.26 Ω cm samples where the control lifetimes are only one order of magnitude higher than the Fe-implanted samples. This observation, coupled with our

**FIG. 5.** Average error as a function of (a) σ_n and σ_p with a fixed $E_t = E_V + 0.2$ eV; (b) σ_p and E_t with a fixed $\sigma_n = 2.3 \times 10^{-14}$ cm².

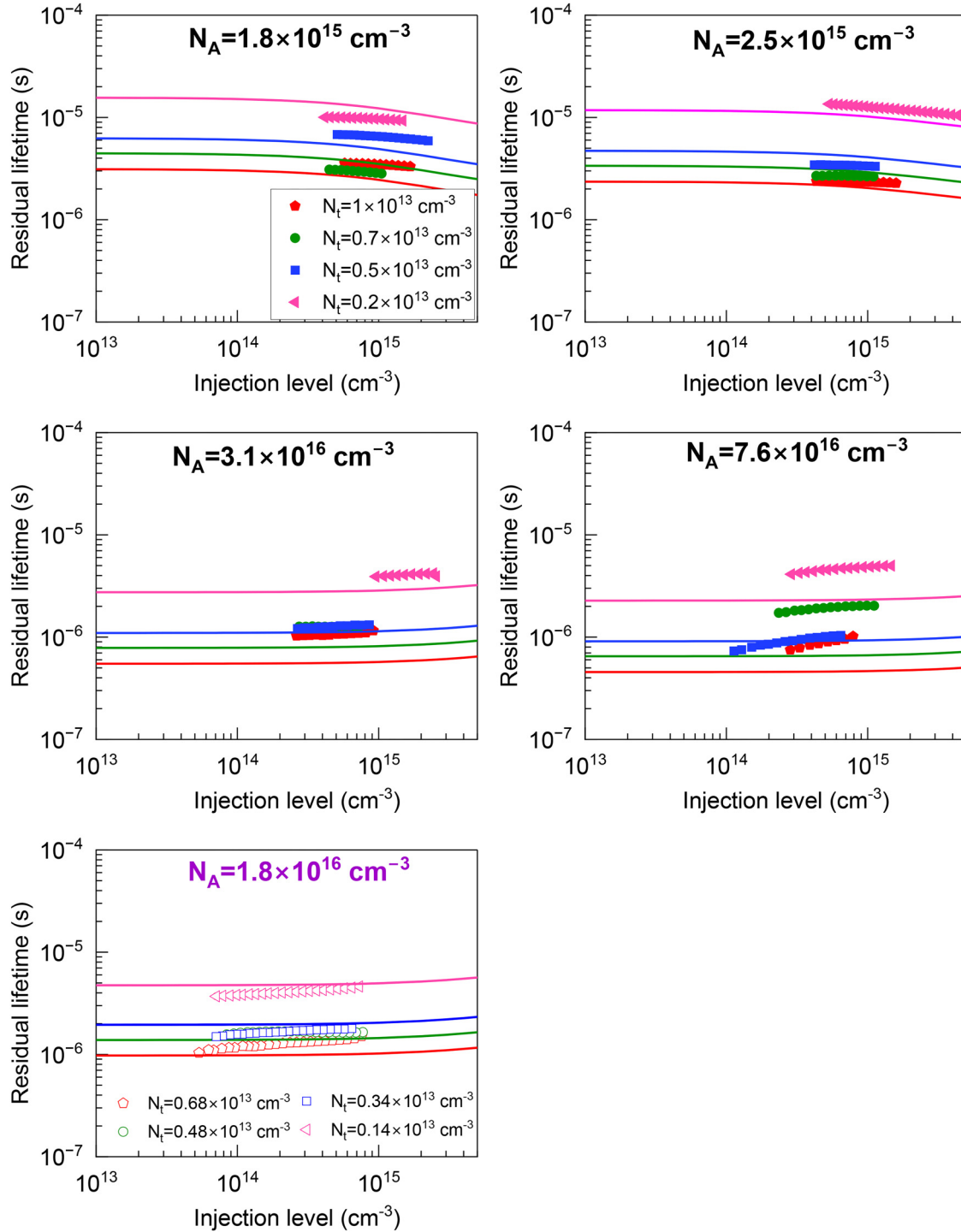


FIG. 6. Experimental residual lifetimes ($\tau_{\text{residual,FeGa}}$), shown as symbols, and simulated SRH lifetimes ($\tau_{\text{SRH,FeGa}}$), shown as solid lines, are plotted as a function of injection level. The simulated $\tau_{\text{SRH,FeGa}}$ are based on the defect parameters from this study. Samples with various combinations of N_A and N_t are shown, including five different N_A values of $1.8 \times 10^{15} \text{ cm}^{-3}$, $2.5 \times 10^{15} \text{ cm}^{-3}$, $1.8 \times 10^{16} \text{ cm}^{-3}$, $3.1 \times 10^{16} \text{ cm}^{-3}$ and $7.6 \times 10^{16} \text{ cm}^{-3}$ and different FeGa concentrations (N_t) ranging from $0.14 \times 10^{13} \text{ cm}^{-3}$ to $1.0 \times 10^{13} \text{ cm}^{-3}$. All of the wafers had a thickness of $170 \pm 10 \mu\text{m}$, except for the sample with a dopant concentration of $N_A = 1.8 \times 10^{16} \text{ cm}^{-3}$, which had a thickness of $230 \pm 10 \mu\text{m}$. With the same surface ion implantation doses but varying wafer thicknesses, different volumetric Fe concentrations were achieved, as listed in the figure labels.

experimental design of purposely implanting Fe into pre-gettered Si wafers, suggests that FeGa should be the primary defect limiting the Si bulk lifetime. Nevertheless, to further ensure the reliability of the “input” lifetime curves for FeGa defect parameterization, lifetime linearization was applied for data filtering, detailed in Sec. III B 1).

Figure 4 also shows the simulated FeGa lifetime curves based on different SRH defect parameters reported in the literature and from this work (summarized in Table I). As shown in Fig. 4, there are clear discrepancies between the experimental and simulated lifetimes using the literature reported values, indicating the need for an improved parameterization. Further details about the defect parameters from this work and the simulation uncertainties will be discussed later in Sec. III B 4.

3. Error analysis by defect parameter contour mapping (DPCM)

As explained earlier in Sec. III A 2, a defect energy level near $E_t = E_V + 0.2$ eV gives a much better fit to the experimental lifetime data in comparison to the level near $E_t = E_V + 0.1$ eV. Therefore, we first undertook a sensitivity analysis by assuming a trap energy level of $E_t = E_V + 0.2$ eV and systematically varying the values of σ_n and σ_p in the range of $1 \times 10^{-12} - 1 \times 10^{-16}$ cm², in order to identify the combination of σ_n and σ_p that yields the minimum average error [from Eq. (3)], as shown in Fig. 5(a).

As evident from Fig. 5(a), while maintaining a fixed energy level $E_t = E_V + 0.2$ eV, the fitting (as represented by the calculated average error) exhibits a strong sensitivity to the input σ_n value. The global minimum average error converges to $\sigma_n = 2.3 \times 10^{-14}$ cm².

Similarly, now with σ_n set at 2.3×10^{-14} cm², we proceeded to explore the dependence of the calculated average error on σ_p and $E_t - E_V$. Once again, a local minimum emerges near $E_t = E_V + 0.2_{-0.01}^{+0.02}$ eV with a value of $\sigma_p = 1.1 \times 10^{-14}$ cm² [Fig. 5(b)].

As shown in Fig. 5(b), the additional fitting narrowed the range of σ_p , although the fitting is still relatively insensitive to σ_p in the range of $3 \times 10^{-15} \leq \sigma_p \leq 1 \times 10^{-14}$ cm². This indicates a limitation in the IDLS approach to extract σ_p for FeGa in Si. Nonetheless, the combination of $\sigma_p = 1.1 \times 10^{-14}$ cm² and $E_t = E_V + 0.2_{-0.01}^{+0.02}$ eV produces the global minimum average error in fitting, and this σ_p value aligns closely with σ_p reported by Post *et al.* from fitting the crossover points of the Fe_i and FeGa lifetime curves.³⁹

In summary, the application of the DPCM analysis yielded the following best-fit FeGa defect parameters: $\sigma_n = 2.3 \times 10^{-14}$ cm², $\sigma_p = 1.1 \times 10^{-14}$ cm², and $E_t = E_V + 0.2_{-0.01}^{+0.02}$ eV. As summarized in Table I, the σ_n and σ_p values are approximately half of the values reported by Schmidt *et al.*⁹ and are close to the results by Post *et al.*³⁹

In Ref. 39, the FeGa defect parameters were extracted from the measured crossover points of the Fe_i and FeGa lifetime curves, based on Fe-implanted silicon wafers with a lower Fe concentration range of $6 \times 10^{10} - 6 \times 10^{11}$ cm⁻³ and a smaller resistivity range of 0.3–3.5 Ω cm. In comparison, the defect parameters from this work mainly came from fitting injection-dependent lifetime curves, and

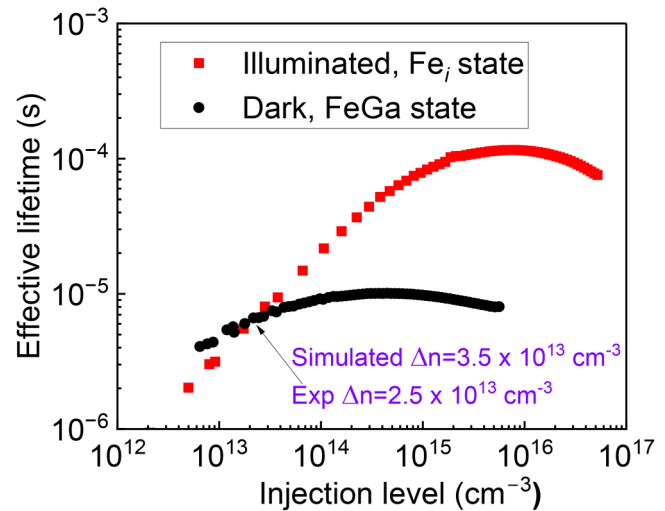


FIG. 7. The effective lifetime curves for both the fully associated state (dark state, FeGa trap) and the fully dissociated state (illuminated state, Fe_i trap) plotted against the excess carrier density for the sample with $N_A = 1.8 \times 10^{15}$ cm⁻³ and $N_t = 0.2 \times 10^{13}$ cm⁻³. The crossover point, as indicated by an arrow in the figure, is where the two lifetimes become equal.

the measured crossover points were used to confirm the results, as will be shown later in Sec. III B 4. N_t in this work was in the range of $1.4 \times 10^{12} - 1.0 \times 10^{13}$ cm⁻³ and samples with a wider range of resistivities (0.26–8.4 Ω cm) were examined. In addition, the pre-gettering step and the lifetime linearization approach helped to rule out the possible interference from other defects. This work, in conjunction with Ref. 39, significantly strengthens the confidence of the reported FeGa defect parameters over a large range of Fe concentration (6×10^{10} cm⁻³– 1.0×10^{13} cm⁻³) and resistivities (0.26–8.4 Ω cm).

4. Comparing experimental and simulated FeGa lifetimes

As shown in Fig. 6, for samples with a wide resistivity range of 8.4–0.55 Ω cm (N_A range from 1.8×10^{15} cm⁻³ to 3.1×10^{16} cm⁻³), the simulated SRH lifetimes (from the defect parameters from this study) show a reasonable agreement with the experimental data. The discrepancies between the simulated and experimental lifetimes throughout the measured injection range are all below 30%.

A larger discrepancy of less than 50% between the simulated and experimental lifetimes was observed for the sample with the lowest resistivity of 0.26 Ω cm. Despite using different mobility models, for a resistivity value of 0.26 Ω cm, the variation in the estimated N_A remains minimal, ranging from 7.1×10^{16} to 7.6×10^{16} cm⁻³.^{43–47} Consequently, the input N_A value cannot explain the larger discrepancy. Instead, the discrepancy may potentially originate from the short diffusion lengths of the lowest resistivity samples, which would lead to larger uncertainties in the experimental lifetime data.^{48–50}

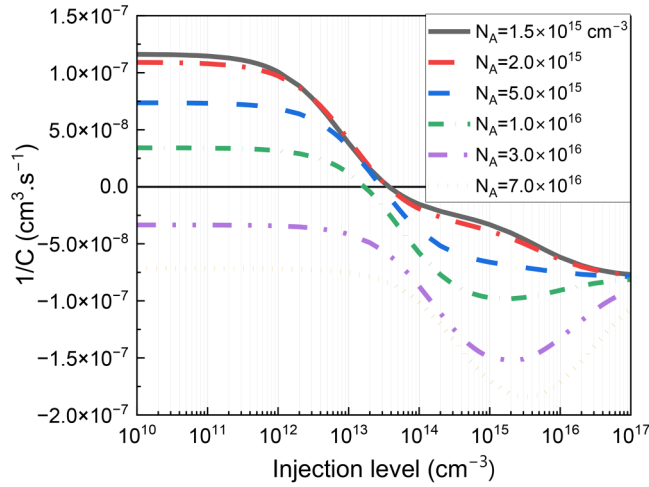


FIG. 8. The inverse of the prefactor ($1/C$) in calculating Fe concentration from Fe_i and FeGa lifetimes [Eq. (4)], is plotted as a function of injection level, for different bulk resistivities. The data shown here are simulations based on the FeGa defect parameters from this study and Fe_i parameters from Ref. 18.

5. Crossover point confirmation of the extracted FeGa recombination parameters

A crossover point, which marks the injection level at which the FeGa associated and dissociated (i.e., Fe_i) lifetimes become equal, $\tau_{SRH, FeGa} = \tau_{SRH, Fe_i}$, serves as a way to verify the extracted defect parameters of FeGa.³⁷ In this work, only a crossover point for the sample with the lowest doping concentration of

$N_A = 1.8 \times 10^{15} \text{ cm}^{-3}$ and $N_t = 0.2 \times 10^{13} \text{ cm}^{-3}$ was observed. The crossover points for other higher dopant samples could not be resolved due to large measurement uncertainty in the low injection range of the IDLS measurements. An example is shown in Fig. 7, where a crossover point was experimentally observed for the sample with $N_A = 1.8 \times 10^{15} \text{ cm}^{-3}$ and $N_t = 0.2 \times 10^{13} \text{ cm}^{-3}$. Employing the FeGa recombination parameters from this work alongside the Fe_i recombination parameters from Istratov *et al.*,¹⁸ the equation of $\tau_{SRH, FeGa} = \tau_{SRH, Fe_i}$ was solved for Δn . The resulting Δn is the simulated crossover point for this sample, at $\Delta n \approx 3.5 \times 10^{13} \text{ cm}^{-3}$. As shown in Fig. 7, this simulated crossover point aligns well with the experimentally measured crossover point at $\Delta n \approx 2.5 \times 10^{13} \text{ cm}^{-3}$. This validates the FeGa recombination parameters found in this work.

6. Application of the new FeGa parameters to $[Fe_i]$ measurement

Similar to FeB,^{36,37} with the knowledge of the recombination parameters of FeGa and Fe_i , the Fe_i concentration in silicon wafers can be determined by Eq. (3).^{9,39} Based on the new FeGa defect parameters from this work and Fe_i parameters from Ref. 18, Fig. 8 plots the inverse of the prefactor ($1/C$) as a function of the injection level for different doping concentrations. Negative values of the parameter C are observed when the injection levels are above the crossover point, indicating an increase in lifetime after FeGa dissociation,⁹ as shown by the example in Fig. 8. This is generally where Fe concentration measurements from conductance-based lifetime measurements take place. Alternatively, techniques such as surface photovoltage typically operate at low injection levels significantly below the crossover point. At low injection levels, the parameter C generally assumes a positive value except for the heavily doped

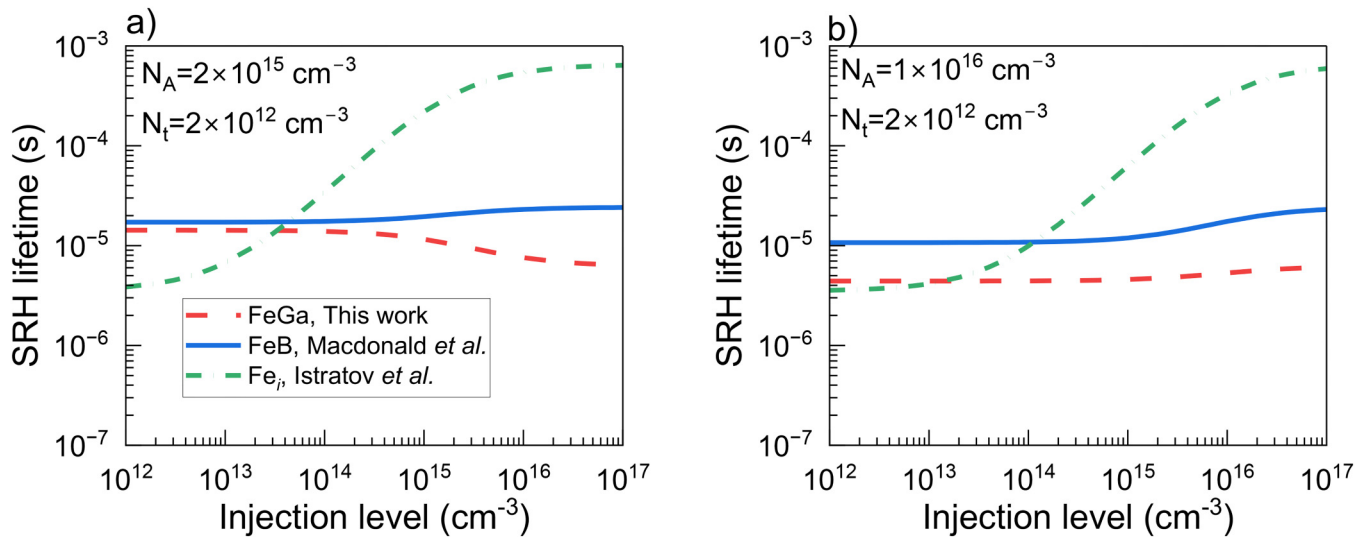


FIG. 9. Simulated injection-dependent SRH lifetime curves based on the defect parameters for Fe_i ,¹⁸ FeB,⁵¹ and FeGa (this work), for two different doping concentrations of (a) $N_A = 2.0 \times 10^{15} \text{ cm}^{-3}$ and (b) $N_A = 2.0 \times 10^{15} \text{ cm}^{-3}$ with the same trap concentration $N_t = 2.0 \times 10^{12} \text{ cm}^{-3}$ on p -type Si at $T = 300 \text{ K}$.

scenario, and C becomes injection-independent at extremely low injection levels.³⁴ The sign change of the prefactor C occurs at $\Delta n \approx 1 \times 10^{13} - 3.5 \times 10^{13} \text{ cm}^{-3}$, which closely aligns with the crossover point in Sec. III B 4.

7. FeGa recombination strength in comparison with Fe_i and FeB

Figure 9 provides a comparison of the simulated SRH lifetimes from FeGa (parameters from this study), Fe_i ,¹⁸ and FeB.⁵¹ The FeGa SRH lifetimes are consistently lower than the FeB lifetimes, indicating that the Fe-acceptor pairs are worse in Ga-doped Si than B-doped Si. The FeGa traps exhibit a notably more detrimental impact on the lifetime above the crossover point of $\tau_{\text{SRH}, \text{Fe}_i}$ and $\tau_{\text{SRH}, \text{FeGa}}$, which occurs at moderate injection levels.

IV. CONCLUSION

This study re-evaluates the FeGa recombination parameters—specifically σ_n , σ_p , and E_t —in Ga-doped silicon wafers with varying resistivities ($8.4\text{--}0.26 \Omega \text{ cm}$) and intentionally implanted iron doses ($0.14 \times 10^{13}\text{--}1.0 \times 10^{13} \text{ cm}^{-3}$), utilizing injection-dependent lifetime spectroscopy (IDLS). The presence of Fe in the test Si wafers was confirmed through monitoring the association kinetics of FeGa and was further corroborated by the detection of interstitial Fe_i by deep-level transient spectroscopy (DLTS). Pre-gettering and lifetime linearization were applied to minimise the influence of other defects on lifetime measurements.

By simultaneous fitting the experimental IDLS data (from samples of varying resistivities and defect concentrations) by the SRH model, the following defect parameters were derived for FeGa in Si: $\sigma_n = 2.3 \times 10^{-14} \text{ cm}^2$, $\sigma_p = 1.1 \times 10^{-14} \text{ cm}^2$, and $E_t = E_V + 0.2^{+0.02}_{-0.01} \text{ eV}$. The results from this study are also in good agreement with the reported values from Schmidt *et al.*⁹ and Post *et al.*³⁹ Finally, the good agreement between the calculated and experimentally measured crossover points of Fe_i and FeGa lifetime curves further validates the recombination parameters of FeGa from this study.

ACKNOWLEDGMENTS

This work was supported by the Australian Renewable Energy Agency (ARENA) through the Australian Centre for Advanced Photovoltaics (ACAP). We acknowledge access to NCRIS funded facilities and expertise at the ion-implantation Laboratory (iiLab), a node of the Heavy Ion Accelerator (HIA) Capability at the Australian National University. We are grateful to Dr Lachlan Black for the fruitful discussion on the effect of different mobility models on the measured IDLS lifetime of the heavily doped samples.

AUTHOR DECLARATIONS

Conflict of Interest

The authors have no conflicts to disclose.

Author Contributions

Tien T. Le: Conceptualization (lead); Data curation (equal); Formal analysis (equal); Investigation (lead); Methodology (equal); Software (lead); Validation (equal); Visualization (equal); Writing – original draft (equal); Writing – review & editing (equal). **Zhuangyi Zhou:** Data curation (equal); Formal analysis (equal); Investigation (equal); Methodology (equal); Resources (equal); Validation (equal); Visualization (equal); Writing – review & editing (equal). **Alan Chen:** Investigation (supporting). **Zhongshu Yang:** Investigation (supporting); Methodology (supporting); Writing – review & editing (supporting). **Fiacre Rougieux:** Project administration (equal); Resources (equal); Supervision (equal); Writing – review & editing (supporting). **Daniel Macdonald:** Conceptualization (equal); Funding acquisition (lead); Project administration (equal); Supervision (lead); Validation (equal); Writing – review & editing (equal). **AnYao Liu:** Conceptualization (lead); Data curation (equal); Formal analysis (equal); Funding acquisition (equal); Investigation (equal); Methodology (equal); Project administration (lead); Resources (equal); Software (equal); Supervision (lead); Validation (equal); Visualization (equal); Writing – original draft (equal); Writing – review & editing (lead).

DATA AVAILABILITY

The data that support the findings of this study are available from the corresponding author upon reasonable request.

REFERENCES

- ¹See <https://itprv.vdma.org/en/ueber-uns> for “International Technology Roadmap for Photovoltaic” (2022).
- ²A. Metz, T. Abe, and R. Hezel, “Gallium-doped Czochralski grown silicon: A novel promising material for the PV-industry,” in *Proceedings of 16th EU PVSEC* (European Photovoltaic Solar Energy Conference, 2000), pp. 1189–1192.
- ³A. R. Meyer, T. O. Abdul Fattah, P. C. Taylor, M. B. Venuti, S. Eley, V. LaSalvia, W. Nemeth, M. Page, D. L. Young, M. Halsall, P. Stradins, and S. Agarwal, “Spectroscopic investigation of shallow hole traps in Ga- and B-doped Czochralski silicon: Insight into light-induced degradation,” *ACS Appl. Energy Mater.* **5**, 13161–13165 (2022).
- ⁴S. W. Glunz, S. Rein, J. Knobloch, W. Wettling, and T. Abe, “Comparison of boron- and gallium-doped p-type Czochralski silicon for photovoltaic application,” *Prog. Photovoltaics Res. Appl.* **7**, 463–469 (1999).
- ⁵R. Basnet, C. Sun, T. Le, Z. Yang, A. Liu, Q. Jin, Y. Wang, and D. Macdonald, “Investigating wafer quality in industrial Czochralski-grown gallium-doped p-type silicon ingots with melt recharging,” *Sol. RRL* **7**(2300304), 1–7 (2023).
- ⁶N. E. Grant, P. P. Altermatt, T. Niewelt, R. Post, W. Kwapil, M. C. Schubert, and J. D. Murphy, “Gallium-doped silicon for high-efficiency commercial passivated emitter and rear solar cells,” *Sol. RRL* **5**(2000754), 1–8 (2021).
- ⁷R. Post, T. Niewelt, W. Kwapil, and M. Schubert, “Carrier lifetime limitation of industrial Ga-doped Cz-grown silicon after different solar cell process flows,” *IEEE J. Photovoltaics* **12**(1), 238–243 (2022).
- ⁸T. Le, Y. Cai, Z. Yang, R. Chen, D. Macdonald, and A. Liu, “Industrial Czochralski n-type silicon wafers: Gettering effectiveness and possible bulk limiting defects,” *Sol. RRL* **8**, 2300928 (2023).
- ⁹J. Schmidt and D. MacDonald, “Recombination activity of iron-gallium and iron-indium pairs in silicon,” *J. Appl. Phys.* **97**(113712), 1–9 (2005).
- ¹⁰T. U. N erland, S. Bernardini, H. Haug, S. Grini, L. Vines, N. Stoddard, and M. Bertoni, “On the recombination centers of iron-gallium pairs in Ga-doped silicon,” *J. Appl. Phys.* **122**(085703), 1–10 (2017).

- ¹¹K. Graff and H. Pieper, "The properties of iron in silicon," *J. Electrochem. Soc.* **128**(3), 669–674 (1981).
- ¹²E. Hvidsten Dahl, V. Osinniy, K. Friestad, A. Soiland, Y. Safir, W. Skorupa, R. Tronstad, and A. Nylandsted Larsen, "Assessing the role of iron-acceptor pairs in solar grade multicrystalline silicon wafers from the metallurgical route," *Phys. Status Solidi* **9**(10–11), 2017–2022 (2012).
- ¹³K. Wünnel and P. Wagner, "Interstitial iron and iron-acceptor pairs in silicon," *Appl. Phys. A Solids Surfaces* **27**(4), 207–212 (1982).
- ¹⁴A. Chantre and L. C. Kimerling, "Trends in the bistable properties of iron-acceptor pairs in silicon," *Mater. Sci. Forum* **10–12**, 387–392 (1986).
- ¹⁵Y. Yoon, Y. Yan, N. P. Ostrom, J. Kim, and G. Rozgonyi, "Deep level transient spectroscopy and minority carrier lifetime study on Ga-doped continuous Czochralski silicon," *Appl. Phys. Lett.* **101**, 222107 (2012).
- ¹⁶S. Beljakowa, D. Karg, G. Pensl, and J. Schmidt, "Degradation of Si-based solar cells caused by CrGa- and FeGa-pairs," in *European Photovoltaic Solar Energy Conference* (2004), pp. 705–708; available at https://www.researchgate.net/publication/241276507_DEGRADATION_OF_SI-BASED_SOLAR_CELLS_CAUSED_BY_CrGa-AND_FeGa-PAIRS/references
- ¹⁷K. Graff, *Metal Impurities in Silicon-Device Fabrication* (Springer, Berlin, 2000), Vol. 24.
- ¹⁸A. A. Istratov, H. Hieslmair, and E. R. Weber, "Iron and its complexes in silicon," *Appl. Phys. A Mater. Sci. Process.* **69**(1), 13–44 (1999).
- ¹⁹D. Macdonald, A. Cuevas, and J. Wong-Leung, "Capture cross sections of the acceptor level of iron-boron pairs in p-type silicon by injection-level dependent lifetime measurements," *J. Appl. Phys.* **89**(12), 7932–7939 (2001).
- ²⁰D. Macdonald, T. Roth, P. N. K. Deenapanray, K. Bothe, P. Pohl, and J. Schmidt, "Formation rates of iron-acceptor pairs in crystalline silicon," *J. Appl. Phys.* **98**, 083509 (2005).
- ²¹J. Tan, D. MacDonald, F. Rougieux, and A. Cuevas, "Accurate measurement of the formation rate of iron-boron pairs in silicon," *Semicond. Sci. Technol.* **26**, 055019 (2011).
- ²²T. F. Cizek and T. H. Wang, "Silicon defect and impurity studies using float-zone crystal growth as a tool," *J. Cryst. Growth* **237–239**, 1685–1691 (2002).
- ²³S. Rein, T. Rehrl, W. Warta, and S. W. Glunz, "Lifetime spectroscopy for defect characterization: Systematic analysis of the possibilities and restrictions," *J. Appl. Phys.* **91**(4), 2059–2070 (2002).
- ²⁴Y. Zhu and Z. Hameiri, "Review of injection dependent charge carrier lifetime spectroscopy," *Prog. Energy* **3**, 012001 (2021).
- ²⁵J. D. Murphy, K. Bothe, R. Krain, V. V. Voronkov, and R. J. Falster, "Parameterisation of injection-dependent lifetime measurements in semiconductors in terms of Shockley–Read–Hall statistics: An application to oxide precipitates in silicon," *J. Appl. Phys.* **111**, 113709 (2012).
- ²⁶D. Macdonald, P. N. K. Deenapanray, and S. Diez, "Onset of implant-related recombination in self-ion implanted and annealed crystalline silicon," *J. Appl. Phys.* **96**(7), 3687–3691 (2004).
- ²⁷A. Liu, D. Yan, S. P. Phang, A. Cuevas, and D. Macdonald, "Effective impurity gettering by phosphorus- and boron-diffused polysilicon passivating contacts for silicon solar cells," *Sol. Energy Mater. Sol. Cells* **179**, 136–141 (2018).
- ²⁸A. Y. Liu, C. Sun, V. P. Markevich, A. R. Peaker, J. D. Murphy, and D. Macdonald, "Gettering of interstitial iron in silicon by plasma-enhanced chemical vapour deposited silicon nitride films," *J. Appl. Phys.* **120**(193103), 193103 (2016).
- ²⁹D. Suh and W. S. Liang, "Electrical properties of atomic layer deposited Al₂O₃ with anneal temperature for surface passivation," *Thin Solid Films* **539**, 309–316 (2013).
- ³⁰A. Y. Liu and D. Macdonald, "Impurity gettering effect of atomic layer deposited aluminium oxide films on silicon wafers," *Appl. Phys. Lett.* **110**(19), 191604 (2017).
- ³¹A. Y. Liu and D. Macdonald, "Impurity gettering by atomic-layer-deposited aluminium oxide films on silicon at contact firing temperatures," *Phys. Status Solidi—Rapid Res. Lett.* **12**(3), 1870309 (2018).
- ³²R. A. Sinton and A. Cuevas, "Contactless determination of current-voltage characteristics and minority-carrier lifetimes in semiconductors from quasi-steady-state photoconductance data," *Appl. Phys. Lett.* **69**(17), 2510–2512 (1996).
- ³³L. E. Black and D. H. Macdonald, "On the quantification of Auger recombination in crystalline silicon," *Sol. Energy Mater. Sol. Cells* **234**(111428), 1–15 (2022).
- ³⁴T. Niewelt, B. Steinhäuser, A. Richter, B. Veith-Wolf, A. Fell, B. Hammann, N. E. Grant, L. Black, J. Tan, A. Youssef, J. D. Murphy, J. Schmidt, M. C. Schubert, and S. W. Glunz, "Reassessment of the intrinsic bulk recombination in crystalline silicon," *Sol. Energy Mater. Sol. Cells* **235**, 111467 (2022).
- ³⁵G. Kemmer and S. Keller, "Nonlinear least-squares data fitting in Excel spreadsheets," *Nat. Protoc.* **5**(2), 267–281 (2010).
- ³⁶G. Zoth and W. Bergholz, "A fast, preparation-free method to detect iron in silicon," *J. Appl. Phys.* **67**(11), 6764–6771 (1990).
- ³⁷D. H. Macdonald, L. J. Geerligs, and A. Azzizi, "Iron detection in crystalline silicon by carrier lifetime measurements for arbitrary injection and doping," *J. Appl. Phys.* **95**(3), 1021–1028 (2004).
- ³⁸S. Leonard, V. P. Markevich, A. R. Peaker, B. Hamilton, and J. D. Murphy, "Evidence for an iron-hydrogen complex in p-type silicon," *Appl. Phys. Lett.* **107**, 032103 (2015).
- ³⁹R. Post, T. Niewelt, W. Yang, D. Macdonald, W. Kwapil, and M. C. Schubert, "Re-evaluation of the SRH-parameters for the FEGA defect," *AIP Conf. Proc.* **2149**, 020012 (2019).
- ⁴⁰H. Lemke, "Energieniveaus und Bindungsenergien von Ionenpaaren in Silizium," *Phys. Status Solidi* **76**, 223–234 (1983).
- ⁴¹M. K. Juhl, F. D. Heinz, G. Coletti, F. E. Rougieux, C. Sun, M. V. Contreras, T. Niewelt, J. Krich, M. C. Schubert, and M. K. Juhl, "On the conversion between recombination rates and electronic defect parameters in semiconductors," *IEEE J. Photovoltaics* **13**(4), 524–534 (2023).
- ⁴²W. M. Bullis and H. R. Huff, "Interpretation of carrier recombination lifetime and diffusion length measurements in silicon," *J. Electrochem. Soc.* **143**(4), 1399–1405 (1996).
- ⁴³P. P. Altermatt, A. Schenk, B. Schmihusen, and G. Heiser, "A simulation model for the density of states and for incomplete ionization in crystalline silicon: II. Investigation of Si:As and Si:B and usage in device simulation," *J. Appl. Phys.* **100**, 113715 (2006).
- ⁴⁴J. M. Dorkel and P. Leturcq, "Carrier mobilities in silicon semi-empirically related to temperature, doping and injection level," *Solid State Electron.* **24**(9), 821–825 (1981).
- ⁴⁵N. D. Arora, J. R. Hauser, and D. J. Roulston, "Electron and hole mobilities in silicon as a function of concentration and temperature," *IEEE Trans. Electron Devices* **29**(2), 292–295 (1982).
- ⁴⁶D. B. M. Klaassen, "A unified mobility model for device simulation—II: Temperature dependence of carrier mobility and lifetime," *Solid State Electron.* **35**(7), 961–967 (1992).
- ⁴⁷D. B. M. Klaassen, "A unified mobility model for device simulation—II: Temperature," *Solid State Electron.* **35**(7), 953–959 (1992).
- ⁴⁸J. S. Swirhun, R. A. Sinton, M. K. Forsyth, and T. Mankad, "Contactless measurement of minority carrier lifetime in silicon ingots and bricks," *Prog. Photovoltaics Res. Appl.* **19**, 313–319 (2011).
- ⁴⁹M. C. Schubert, M. J. Kerler, and W. Warta, "Influence of heterogeneous profiles in carrier density measurements with respect to iron concentration measurements in silicon," *J. Appl. Phys.* **103**, 073710 (2008).
- ⁵⁰T. T. Le, S. P. Phang, Z. Yang, D. Macdonald, and A. Liu, "Impact of depth-wise inhomogeneous iron distributions on the accuracy of lifetime-based interstitial iron measurements on silicon wafers," *IEEE J. Photovoltaics* **13**(4), 495–502 (2023).
- ⁵¹J. E. Birkholz, K. Bothe, D. MacDonald, and J. Schmidt, "Electronic properties of iron-boron pairs in crystalline silicon by temperature- and injection-level-dependent lifetime measurements," *J. Appl. Phys.* **97**, 103708 (2005).